Appl. Phys. A (2016) 122:853
DOI 10.1007/s00339-016-0389-9

Applied Physics A
Materials Science & Processing

Controllable growth of vertically aligned Bi-doped TiO_2 nanorod arrays for all-oxide solid-state DSSCs

Morteza Asemi[1,2] · **Majid Ghanaatshoar**[1,2]

Received: 21 August 2016 / Accepted: 22 August 2016 / Published online: 27 August 2016

Abstract In this study, vertically aligned Bi-doped TiO_2 nanorod arrays as photoanodes were successfully grown on the fluorine-doped tin oxide by hydrothermal method. Structural analysis showed that bismuth was successfully incorporated into the TiO_2 lattice at low concentration, but at higher concentration, phase segregation of Bi_2O_3 in the TiO_2 matrix was occurred. TiO_2 nanorods with 3 % bismuth concentration had minimum electrical resistivity. As the solid-state electrolyte, Mg-doped $CuCrO_2$ nanoparticles with *p*-type conductivity were synthesized by sol–gel method. The fabricated all-oxide solid-state dye-sensitized solar cells with Bi-doped TiO_2 nanorods displayed better photovoltaic performance due to the presence of Bi. The improved cell performance was correlated with the higher dye loading, slower charge recombination rate and the higher electrical conductivity of the photoanodes. After mechanical pressing, the all-oxide solid-state DSSC exhibited enhanced photovoltaic performance due to the formation of the large neck between adjacent nanoparticles by mechanical sintering. The open-circuit photovoltage decay measurement of the devices and electrical conductivity of the nanoparticles before and after pressing revealed that the mechanical pressing technique reduces charge recombination rate and facilitates electron transport through the interconnected nanoparticles.

✉ Majid Ghanaatshoar
m-ghanaat@sbu.ac.ir

[1] Laser and Plasma Research Institute, Shahid Beheshti University, G.C., Evin, 1983969411 Tehran, Iran

[2] Solar Cells Research Group, Shahid Beheshti University, G.C., Evin, 1983969411 Tehran, Iran

1 Introduction

In comparison with other renewable energy sources, solar energy has been regarded as one of the most important sources due to its unique advantages such as abundance, availability and predictability [1, 2]. Among the different types of the photovoltaic devices which convert solar energy directly into electricity, dye-sensitized solar cells (DSSCs) have attracted a great deal of attention over the past decades due to their simple fabrication process, low production cost and high power conversion efficiencies [3–5]. Although power conversion efficiency up to 13 % has been successfully reported for DSSCs by employing molecularly engineered zinc porphyrin dye, coded SM315, in conjunction with organic liquid-based electrolyte containing cobalt (II/III) redox couple [6], there are a number of scientific and technological problems such as dye degradation, electrode corrosion, solvent flammability, leakage and volatilization of organic liquid electrolytes for widespread commercialization and long-term practical application of DSSCs [7–10]. Among the aforementioned problems, the leakage and evaporation of the liquid electrolytes have been recognized as the most restrictive factors in sealing which prevent the long-term outdoor applications of DSSCs [11]. To overcome these problems, considerable efforts have been paid to develop quasi-solid-state or solid-state electrolytes for construction of solid-state DSSCs [12–14]. Several types of quasi-solid-state or solid-state electrolytes including organic and inorganic hole conductors, *p*-type semiconductors, physically cross-linked gelators and polymer gel electrolytes have been proposed as credible alternatives to conventional liquid electrolytes [15–20]. However, the efficiency of DSSCs fabricated with these electrolytes is still unsatisfactory in comparison with liquid-based electrolytes due to their

relatively lower ionic conductivity and poor electrolyte/electrode interfacial contact [13, 16].

Insufficient pore-filling of the mesoporous photoanodes by solid-state electrolytes has been identified as a main reason for low efficiency of solid-state DSSCs [15, 21]. In order to fill the pores of the ZnO photoanode with *p*-type semiconductor, Gratzel et al. have deposited CuSCN *p*-type semiconductor by electrochemical deposition method to fabricate solid-state ZnO/dye/CuSCN solar cells [22]. This method can be considered as a perfect way to fill the pores of the dye-coated photoanode with a *p*-type semiconductor, but because of the dye degradation, it is not applicable. Sirimanne et al. and Premalal et al. have employed 1-methyl-3-ethyl-imidazolium thiocyanate (MEIT) and triethylamine hydrothiocyanate (THT) as chelating agent in the coating solution of the CuI to improve the efficiency of CuI-based solid-state dye-sensitized solar cells, respectively [23, 24]. In these cases, chelating agents prevent the crystal growth of CuI during the deposition process and control the crystal size of *p*-type CuI. Furthermore, at the same time, CuI has enough time for filling the pores of the TiO_2 photoanode. Recently, Nejati and Lau [25] have presented initiated chemical vapor deposition (iCVD) as a solvent-free method to polymerize poly (2-hydroxyethyl methacrylate) (PHEMA) inside the mesoporous TiO_2 photoanode. In this technique, polymerization and deposition of poly (2-hydroxyethyl methacrylate) can be performed in a single step by controlling the physical and chemical parameters which affect the rate of polymerization inside the pores. Infiltration of spiro-OMeTAD into mesoporous TiO_2 photoanode has also been performed by deposition of spiro-OMeTAD solution on the dye-coated TiO_2 photoanode using spin-coating technique [26]. In this way, spiro-OMeTAD solution can be effectively penetrated into the pores of the photoanode.

P-type metal-oxide-semiconductors with delafossite-type structure have been found to be good candidates for hole transport materials in solid-state DSSCs [17]. Difficulty in penetration of $CuAlO_2$ nanoparticles into mesoporous structure of the photoanode due to the large particle size and then weak interaction of N719 dye molecules with $CuAlO_2$ nanoparticles as a hole transport material and low conductivity of the $CuAlO_2$ nanoparticles have been recognized as the reasons for the poor performance of the fabricated solid-state DSSCs. Among the *p*-type wide-band-gap semiconductors with delafossite structure which are applicable in DSSCs, Mg-doped $CuCrO_2$ nanoparticles have higher conductivity compared with others [27]. Unfortunately, to obtain a wide-band-gap metal-oxide-semiconductor with desirable properties (such as crystalline structure, high electrical conductivity and transparency in visible region), high-temperature annealing is required during the synthesis process which is undesirable for DSSCs (due to the dye degradation). To solve this problem, in a previous work, we initially synthesized undoped and metal-doped $CuCrO_2$ nanoparticles separately [28]. For better penetration into TiO_2 photoanode, $CuCrO_2$ nanoparticles have been dispersed in ethanol and used as electrolyte. Finally, by evaporation of ethanol at room temperature, the solid-state electrolyte has been obtained.

In the present work, vertically aligned Bi-doped TiO_2 nanorod arrays were grown on the FTO substrate for the first time and then were used as photoanode to fabricate all-oxide solid-state DSSCs. Vertically aligned TiO_2 nanorod arrays due to having direct pathway for penetration of solid-state electrolyte in the gap between the nanorods were selected. In addition, the electrical conductivity of the TiO_2 nanorods with Bi doping can be improved and facilitated for photo-generated electron transportation. Furthermore, in order to fill the gap between the nanorods with small-size Mg-doped $CuCrO_2$ nanoparticles, prepared nanoparticles were grinded in a planetary ball mill. Moreover, to improve the interconnection between the nanoparticles, the constructed all-oxide solid-state DSSCs were pressed with hydraulic press under constant pressure. It can be predicted that the performance of the all-oxide solid-state DSSCs can be enhanced by improving the conductivity of the TiO_2 nanorods by Bi doping and increasing the interconnection between the nanoparticles and reaching the high degree of pore-filling by pressing. Finally, the photovoltaic properties of the fabricated all-oxide solid-state DSSCs were investigated.

2 Experimental methods

The vertically aligned Bi-doped TiO_2 nanorod arrays were grown on fluorine-doped tin oxide (FTO) transparent conductive oxide glass by hydrothermal method. Firstly, FTO glass substrates ($1.5 \times 2.0\ cm^2$) were cleaned by ethanol, acetone and deionized water in an ultrasonic bath for 30 min, dried in air at room temperature and then were placed into a Teflon-lined stainless steel autoclave (100 ml volume). Then, 15 ml deionized water was mixed with 15 ml hydrochloric acid (HCl, Amertat Shimi Co., Iran) under magnetic stirring at room temperature. After stirring for 10 min, 0.55 ml titanium tetraisopropoxide (TTIP, Samchun Chemical Co., Korea) accompanied with different values of bismuth (III) nitrate pentahydrate ($Bi(NO_3)_3{\cdot}5H_2O$, Chem-Lab NV Co., Belgium) as dopant source was slowly added to the mentioned mixed solution and stirred vigorously for 20 min to obtain a transparent solution. Afterward, the obtained transparent solution was transferred into the Teflon-lined stainless steel autoclave. The sealed autoclave was placed into an electric furnace (F35L-1200, Azar Furnace Co., Iran) at 160 °C for 12 h.

After the reaction, the Teflon-lined stainless steel autoclave was cooled down naturally to room temperature and the grown vertically aligned Bi-doped TiO_2 nanorod arrays on the FTO glass were taken out, rinsed with deionized water and ethanol for several times and finally dried in air at room temperature. In order to increase the length of the Bi-doped TiO_2 nanorods, the hydrothermal process was repeated for several times using fresh solution.

$CuCrO_2$ nanoparticles with Mg doping concentration of 5.0 at.% were prepared by sol–gel method. Copper acetate monohydrate ($Cu(CH_3COO)_2{\cdot}H_2O$, Merck Co., Germany) and chromium nitrate nonahydrate ($Cr(NO3)_3{\cdot}9H_2O$, Merck Co., Germany), magnesium nitrate hexahydrate ($Mg(NO_3)_2{\cdot}6H_2O$, Merck Co., Germany) and 2-methoxyethanol ($CH_3(CH_2)_2OOH$, Merck Co., Germany) were used as starting materials, dopant source and solvent, respectively. The molar ratio of [Cu]/[Cr+Mg] was fixed at 1.0, and the concentration of copper acetate in the solution was maintained to be 0.7 M. The precursor solution was prepared by dissolving copper acetate monohydrate, chromium nitrate nonahydrate and magnesium nitrate hexahydrate in 2-methoxyethanol at 60 °C. The obtained solution was stirred in a magnetic stirrer at 60 °C for 3 h to obtain a deep green, transparent and homogenous solution. The resultant solution was dried at 110 °C for 3 h. Finally, the dried powder was heat-treated in an electric furnace in air at 900 °C for 1 h. In order to produce fine and homogenous particles, after annealing, the powder was milled in a planetary ball-milling machine (NARYA MPM-2*250 H, Amin-Asia Co., Iran) at 400 rpm for 5 h in a zirconia vessel and with zirconia balls in ethanol. The ball-to-powder ratio weight was 10:1.

The prepared Bi-doped TiO_2 nanorod arrays on FTO glass substrate were used as photoanode for dye-sensitized solar cells. Prior to dye sensitization, the as-prepared Bi-doped TiO_2 nanorod arrays were heated at 150 °C for 30 min. After cooling down to 80 °C, the Bi-doped TiO_2 electrodes were immersed into 0.5 mM N719 dye (Dyesol Co., Australia) solution in ethanol, kept for 24 h at room temperature and then rinsed with ethanol and dried in air. Subsequently, Mg-doped $CuCrO_2$ nanoparticles were dispersed in ethanol and deposited on the surface of the dye-coated Bi-doped TiO_2 nanorod arrays using a spincoater (SC-410 spincoater, Backer Viera Trading Co., Iran) at spin speed of 1000 rpm for 30 s. Furthermore, the Pt-coated FTO glass substrate as a counter electrode was prepared by spin coating of H_2PtCl_6 solution (5 mM in 2-propanol) at 500 rpm for 10 s and then heat-treated at 450 °C for 30 min in air. The active area of the dye-coated Bi-doped TiO_2 nanorods was 0.2 cm^2. The sensitized Bi-doped TiO_2 photoanode and the Pt-coated FTO counter electrode were assembled in a sandwich-type solar cell. Finally, to improve the interconnection between the nanoparticles and the penetration of a large amount of the nanoparticles into the photoanode, the constructed all-oxide solid-state DSSCs were pressed by hydraulic press (769YP-15A, Tianjin Keqi High and New Technology Co., China) under constant pressure (5 MPa) at room temperature for 30 min.

The crystalline structure of the synthesized undoped and Bi-doped TiO_2 nanorod arrays and Mg-doped $CuCrO_2$ nanoparticles was characterized by an X-ray diffractometer (XRD, STOE STADI-P Co., Germany) using CuKα radiation ($\lambda = 0.15406$ nm), and the crystallite size was calculated by Debye–Scherrer's formula. The surface morphology of the prepared nanorod arrays and Mg-doped $CuCrO_2$ nanoparticles was examined by a Hitachi S-4100 field emission scanning electron microscopy (FESEM) and a TESCAN MIRA 3 XMU FESEM, respectively. The length of the vertically aligned Bi-doped TiO_2 nanorods was also determined by cross-sectional FESEM. In addition, the transmission electron microscopy (TEM) was carried out using a Zeiss EM10C microscope operating with an accelerating voltage of 100 kV to estimate the size of the nanoparticles. The electrical conductivity of the nanorods and nanoparticles (before and after pressing) was measured in the van der Pauw configuration using a four-point probe setup by applying voltage and measuring the current. The UV–Vis absorption spectroscopy of the desorbed-dye solutions was performed by a UV–Vis spectrophotometer (AvaSpec-3648, Avantes Co., Netherlands) using a quartz cuvette with 1-cm path length. The current density–voltage (J–V) measurements of the fabricated all-oxide solid-state DSSCs were carried out under illumination of an AM1.5 solar simulator (SIM-1000, Sharif Solar Co., Iran) using an I–V tracer (IV-25, Sharif Solar Co., Iran). The intensity of simulated solar light was calibrated with a standard crystalline silicon solar cell. The open-circuit photovoltage decay measurement was performed by recording the decay of the photovoltage as a function of time after turning off the light in open-circuit condition.

3 Results and discussion

The XRD patterns of the undoped and Bi-doped TiO_2 nanorods with various levels of bismuth doping concentration grown on FTO glass substrate are presented in Fig. 1. The XRD patterns of the nanorods are in good agreement with the rutile phase of the TiO_2 (JCPDS Card No. 00-001-1292) [28, 29]. There are no obvious peaks of Bi metal clusters, Bi oxides or secondary phases in the samples where the doping level is lower than 3 %. This signifies that Bi ions are successfully incorporated into the TiO_2 lattice during the synthesis process. However, when the doping level of Bi increases to above 3 %,

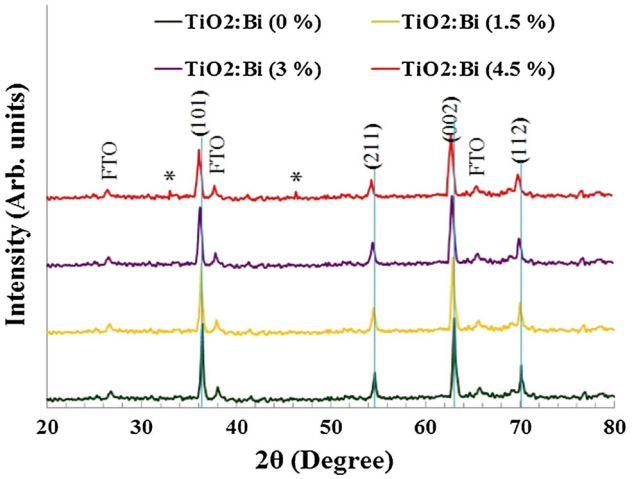

Fig. 1 X-ray diffraction patterns of undoped and Bi-doped TiO_2 nanorod arrays on FTO glass substrates. Peaks labeled as * are attributed to the Bi_2O_3 structure. The solid lines are guide for the eyes

characteristic peaks of the crystalline Bi_2O_3 appear (JCPDS Card No. 00-001-0709) [30]. Furthermore, the position of the diffraction peaks of Bi-doped TiO_2 nanorods is slightly shifted toward lower angles with increasing Bi concentration. Wang et al. and Hamedani et al. reported similar shift in Ti-doped SnO_2 and Sr-doped TiO_2 nanotube arrays, respectively [31, 32]. In general, as the doping concentration increases, the lattice parameters of the host material change according to Vegard's law due to the generation of strain in the crystal lattice of the host material and the diffraction peaks shift toward higher or lower angles with regard to the ionic radius of the dopant [31, 32]. In addition to the shift of the peaks, the intensity of the diffraction peaks of TiO_2 nanorods is decreased and their full width at half maximum (FWHM) is increased with Bi doping concentration. The Debye–Scherrer's equation confirms that the Bi doping has obviously affected the crystallite size of the TiO_2 nanorods. The crystallite size of the TiO_2 nanorods has decreased from 25.9 to 17.4 nm in the (002) orientation with increasing dopant concentration. It means that the crystallinity of the Bi-doped TiO_2 nanorods is slightly declined. The decrease in crystalline quality of the doped TiO_2 nanorods can be attributed to the lattice disorder and stress due to the larger ionic radius of Bi^{3+} ions (1.030 Å) compared with Ti^{4+} ions (0.605 Å). According to the XRD patterns, we can conclude that the optimal doping concentration of Bi in TiO_2 structure is about 3 % in our experiments.

Top-view FESEM images of undoped and Bi-doped TiO_2 nanorod arrays grown on FTO glass substrates are shown in Fig. 2. This figure shows that the surface of the FTO substrates has been uniformly covered by discrete vertically aligned nanorods. Furthermore, as can be seen, average diameter of the nanorods has increased with increasing Bi doping concentration. Xiao et al. [33] reported similar increase in the diameter of the ZnO nanorods with Fe doping. In addition, the morphology changes of the ZnO nanowire/nanotube with variation of the initial solution concentration were previously reported by Liang et al. [34], which were described by the dislocation-driven growth process. The increase in the diameter of the TiO_2 nanorods with bismuth doping concentration can be understood by this growth mechanism. Bismuth doping has similar influence on the supersaturation degree of the growth solutions. The length of the synthesized TiO_2 nanorod arrays is about 3.5 μm for both undoped and Bi-doped samples. In order to increase the length of the vertically aligned Bi-doped TiO_2 nanorod arrays, the procedures of the nanorods growth are repeated two, three and four times. Figure 3 shows the cross-sectional FESEM images of first, second and third growth steps of the synthesized nanorods. The length of the Bi-doped TiO_2 nanorod arrays is about 6 and 7.5 μm for the second and third growth steps, respectively. With increasing the growth steps above three times, the grown nanorods on the surface of the FTO glass substrates are detached from the substrates. The peeling of the TiO_2 nanorods from the FTO substrate has been previously observed by Liu et al. [29].

Figure 4 shows that the diffraction peaks of the prepared nanoparticles are indexed to a delafossite structure of $CuCrO_2$ (JCPDS Card No. 01-089-6744) [35]. As shown in this figure, it is obvious that there is no extra peak due to magnesium, which indicates that Mg ions have been uniformly incorporated into the host lattice of $CuCrO_2$ crystals. The previous studies have shown that the substitution of 5 % Mg^{2+} in Cr^{3+} site significantly improves the *p*-type electrical conductivity of the $CuCrO_2$ nanoparticles due to the creation of free holes [28]. The average crystallite size of the nanoparticles is about 37.7 nm in (006) direction. According to this value, it is realized that the nanoparticles are relatively large, and for a better penetration of the nanoparticles in the space between the nanorods, their size should be reduced. Figure 5 shows the FESEM and TEM images of the synthesized Mg-doped $CuCrO_2$ nanoparticles after ball milling for 5 h. This figure illustrates that the morphology of most of the Mg-doped $CuCrO_2$ nanoparticles is spherical in shape and their average size after ball milling is around 17 nm.

The current density–voltage (J–V) curves of the fabricated SS-DSSCs with Bi-doped TiO_2 nanorods as photoanode and Mg-doped $CuCrO_2$ nanoparticles as solid-state electrolyte are shown in Fig. 6a. Their photovoltaic parameters are also summarized in Table 1. As shown in Fig. 6a, the efficiency of the devices initially increases with increasing the Bi doping concentration to reach 3 %. At this condition, the short-circuit current density (J_{SC}), open-circuit voltage (V_{OC}) and power conversion efficiency (η)

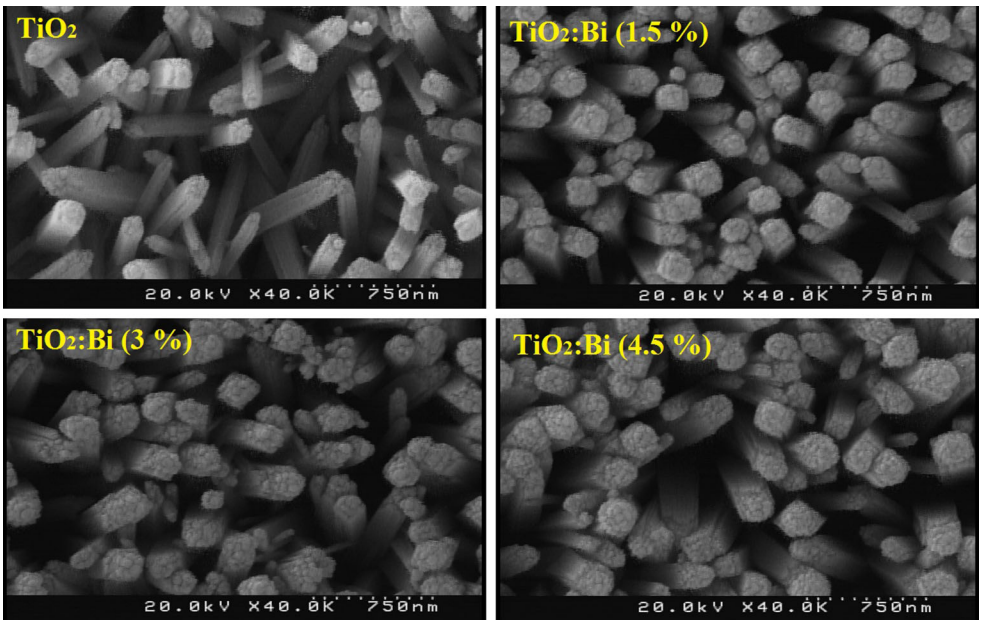

Fig. 2 Top-view FESEM images of as-grown undoped and Bi-doped TiO_2 nanorod arrays with 1.5, 3 and 4.5 % Bi doping concentration

of the constructed all-oxide solid-state DSSCs are 724 μA/cm^2, 342 mV and 0.102 %, respectively. When the concentration of the Bi dopant goes beyond 3 %, the performance of the device is deteriorated. For instance, J_{SC}, V_{OC} and η of the solid-state DSSC made from the nanorods with Bi dopant concentration of 4.5 % decreases to 693 μA/cm^2, 320 mV and 0.081 %, respectively. The observed variation with Bi dopant concentration in the photovoltaic performance of the all-oxide solid-state DSSCs can be due to the following reasons:

1. The increase in the Bi dopant concentration initially increases the electrical conductivity of the doped TiO_2 nanorods. When a small amount of Bi is introduced into the TiO_2 structure, the Bi^{+3} placed in Ti^{+4} sites is ionized and then oxygen vacancy sites are created in the TiO_2 structure. This can improve the transportation of the photo-generated electrons in the device [36]. However, if the Bi dopant concentration is increased to above 3 %, the transportation of the photo-generated electrons in the device is declined because of the crystallinity deterioration of the doped TiO_2 (see Fig. 1). In order to study the electrical conductivity of the prepared nanorod arrays, the current–voltage characteristics of the TiO_2 nanorod arrays grown on the FTO glass substrates are compared in Fig. 6b. The graphical configuration of the prepared samples for I–V measurement is represented in the inset of Fig. 6b. The I–V characteristics of all the samples exhibit ohmic contact behavior and verify our statement about the electrical conductivity of the prepared nanorods. As shown in Table 1, the electrical resistivity strongly depends on the bismuth content. The improvement in the electrical conductivity of the TiO_2 nanorods can be due to the substitution of the Bi atoms on the Ti atoms site. Previously, Zuo et al. [37] reported electrical conductivity enhancement in Bi-doped TiO_2 nanoparticles prepared by the sol–gel method. For further investigation, we carried out the open-circuit photovoltage decay (OCVD) measurement to study the effect of the electrical conductivity improvement in the recombination kinetics. The OCVD measurement is known as one of the most important characterization techniques to study the recombination kinetics in the DSSCs [38]. In order to perform this measurement, the fabricated solid-state DSSC is illuminated with simulated solar light and a steady state photovoltage is obtained. Then, at open-circuit condition, the decay of the photovoltage as a function of time is recorded after turning off the light. At open-circuit condition under illumination of simulated AM1.5 solar light, the electron photo-generation rate is equal to the recombination rate of the photo-generated electrons. When the electron photo-generation process is stopped by turning off the light, the injected electrons in the conduction band of photoanode start to decay due to the recombination [38–40]. As shown in Fig. 6c, the decay of V_{OC} in Bi-doped TiO_2-nanorod-based all-oxide solid-state DSSCs is slower than that made from undoped TiO_2 nanorods, which indicates a faster electron transport process in Bi-doped TiO_2 nanorods.
2. The enhancement of dye loading on the surface of the Bi-doped TiO_2 nanorods compared with undoped TiO_2

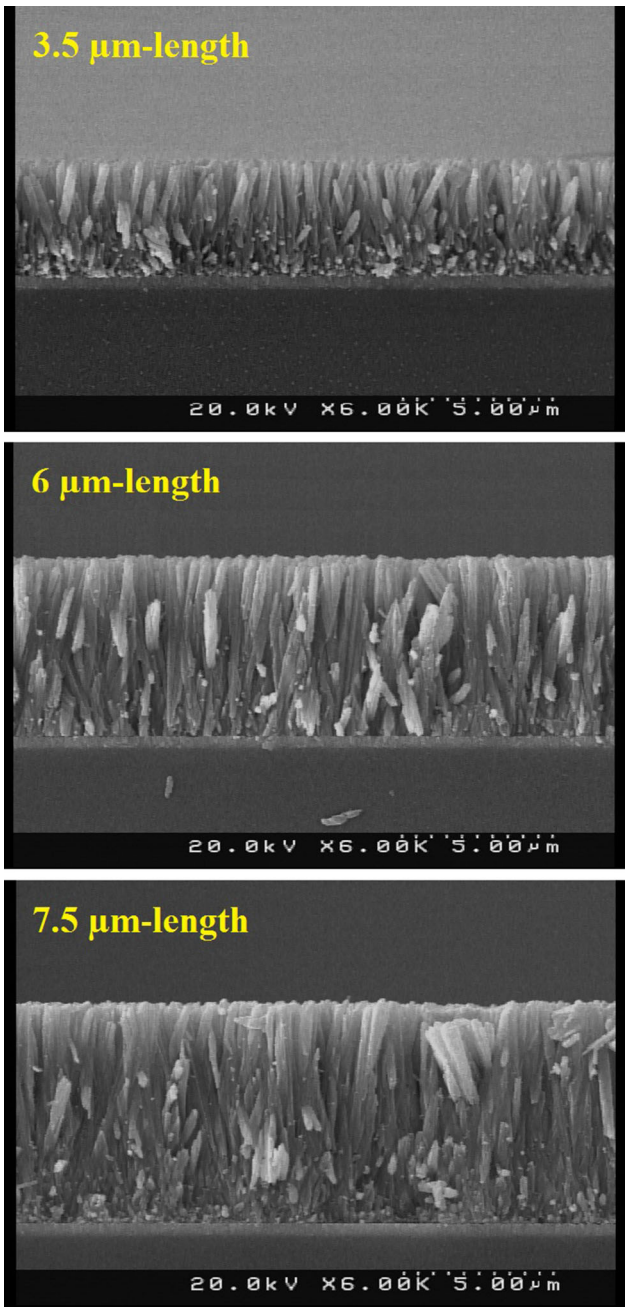

Fig. 3 Cross-sectional FESEM images of TiO_2 nanorod arrays on FTO glass substrates

nanorods at the same thickness can improve the photovoltaic performance of the all-oxide solid-state DSSCs. To verify this, dye-loading measurements were performed by immersing dye-attached undoped and Bi-doped TiO_2 nanorods in 0.1 M NaOH solution of water [41]. The measured UV–Vis absorption spectra of each desorbed-dye solution are shown in Fig. 6d. The obtained results reveal that the intensity of the absorbance peak at 510 nm, originating from the N719 dye molecules, is larger for the Bi-doped TiO_2 nanorod-

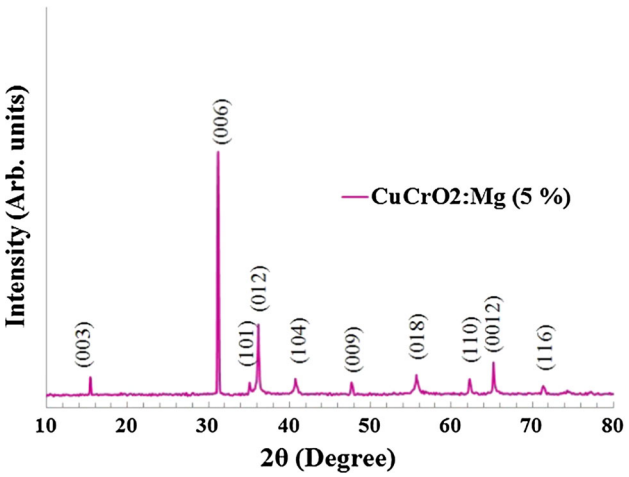

Fig. 4 X-ray diffraction patterns of Mg-doped $CuCrO_2$ nanoparticles

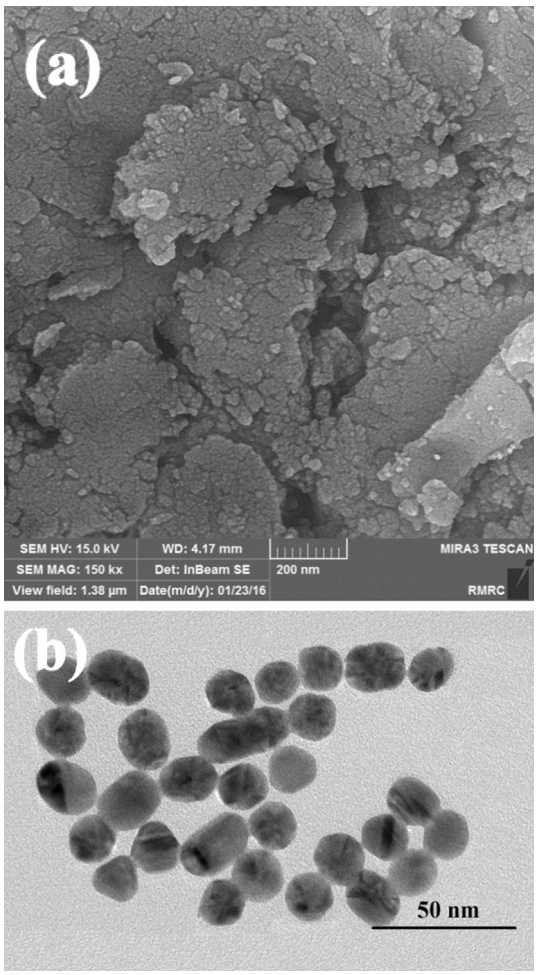

Fig. 5 **a** FESEM and **b** TEM images of the synthesized Mg-doped $CuCrO_2$ nanoparticles after ball milling for 5 h

based photoanodes in comparison with that of the undoped TiO_2-based one. The higher dye loading on the surface of the Bi-doped TiO_2 nanorods can be attributed

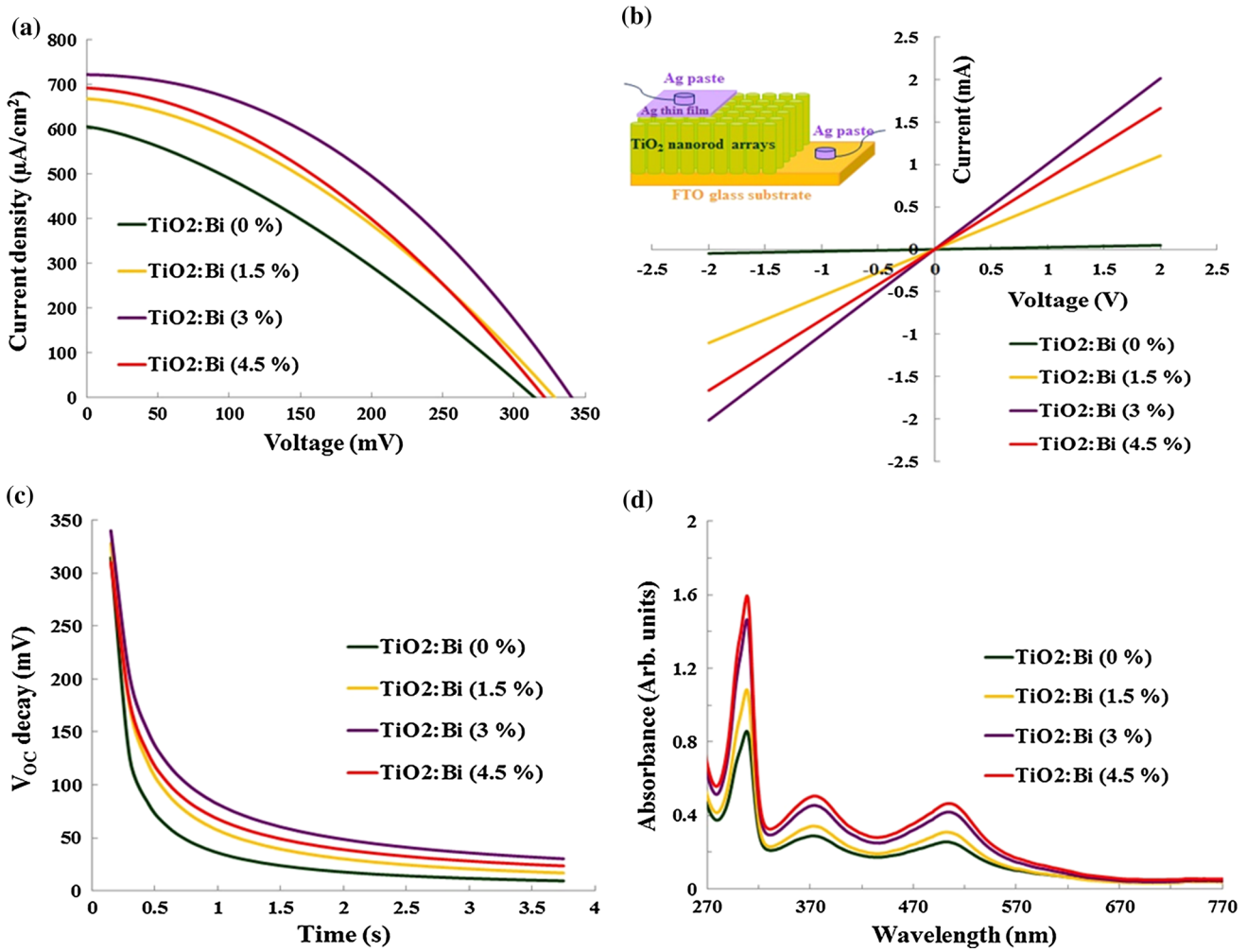

Fig. 6 **a** Current density–voltage characteristics of the solid-state DSSCs made from undoped and Bi-doped TiO_2 nanorods under simulated AM1.5 solar light (100 mW/cm^2), **b** I–V curves of the prepared nanorod arrays on FTO substrates, **c** open-circuit photovoltage decay measurements of the fabricated solid-state DSSCs and **d** UV–Vis absorption spectra of the desorbed N719 dye molecules from the photoanodes

Table 1 Photovoltaic parameters of the fabricated solid-state DSSCs with different photoanodes

Electrode	R (kΩ)	J_{SC} (μA/cm^2)	V_{OC} (mV)	FF (%)	η (%)
TiO_2/Bi (0 %)	41.65	607	313	32.1	0.061
TiO_2/Bi (1.5 %)	1.82	670	328	35.6	0.078
TiO_2/Bi (3 %)	0.98	724	342	39.8	0.102
TiO_2/Bi (4.5 %)	1.21	693	320	36.5	0.081

to the rougher surface of the doped nanorod tips and higher density of the nanorods on the FTO substrate, which increase the specific area of the prepared photoanodes (see Fig. 2). Therefore, the Bi doping not only improves the electrical conductivity of the TiO_2 nanorods but also enhances their dye loading. The enhancement of the dye loading on the surface of the TiO_2 nanotubes by Ru doping was previously reported by So et al. [42]. In addition, Liu et al. [43] reported similar results for TiO_2 nanoparticles by Ta doping.

The performance of the DSSCs can be improved by increasing the length of the nanorods. The J–V characteristics of the all-oxide solid-state DSSCs made from Bi-doped TiO_2 (3 %) nanorod arrays with various lengths are displayed in Fig. 7a. The efficiency of the SS-DSSCs increases progressively with increasing the length of the nanorod arrays. The solid-state DSSC fabricated from a 7.5-μm-long Bi-doped TiO_2 nanorod arrays shows better performance with J_{SC} of 890 μA/cm^2, V_{OC} of 348 mV and power conversion efficiency of 0.120 % compared to the

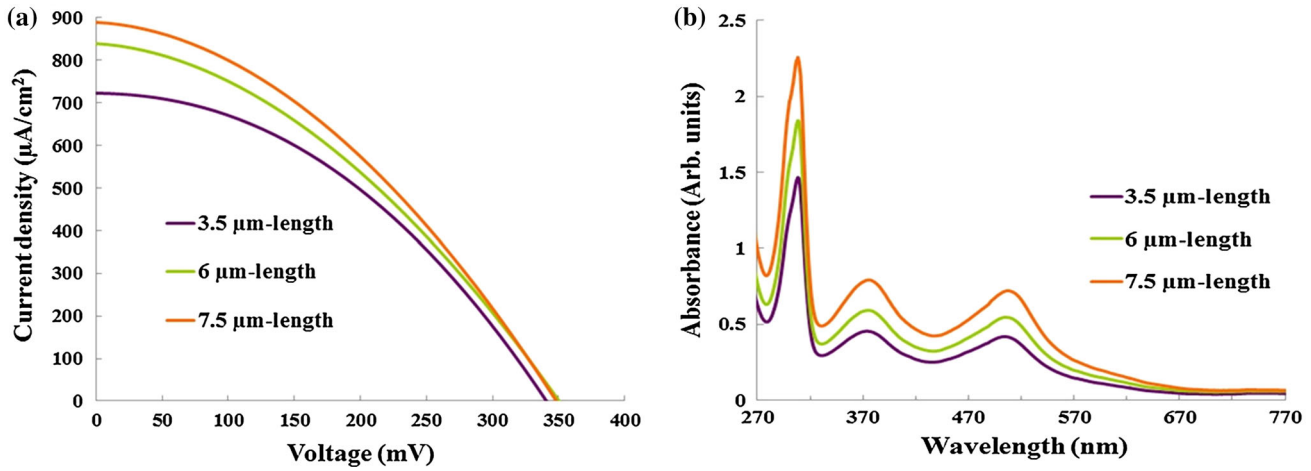

Fig. 7 **a** Current density–voltage characteristics of the solid-state DSSCs made from the Bi-doped TiO_2 (3 %) nanorods with different lengths under simulated AM1.5 solar light (100 mW/cm^2) and **b** UV–Vis absorption spectra of the N719 dye molecules desorbed from TiO_2 photoanodes

Table 2 Photovoltaic parameters of the solid-state DSSCs made from the Bi-doped TiO_2 (3 %) nanorods with different lengths

Electrode	J_{SC} (μA/cm^2)	V_{OC} (mV)	FF (%)	η (%)
3.5 μm length	724	342	39.8	0.102
6 μm length	840	349	37.1	0.109
7.5 μm length	890	348	36.8	0.120

two other samples. As shown in Table 2, the enhancement of the conversion efficiency is mainly due to the increase in the short-circuit current. The increase in J_{SC} with nanorod length can be ascribed to the enlarged surface area of the nanorod arrays and hence the amount of adsorbed dye on the nanorods' surface. The absorption spectrum of the desorbed dye from the photoanodes represents that the amount of adsorbed dye on the surface of the 7.5-μm-long Bi-doped TiO_2 nanorod arrays photoanode is higher than that adsorbed on the surface of the photoanode made from the other nanorods (see Fig. 7b). The dye adsorption enhancement for the enlarged nanorods has also been reported for ZnO [44]. As the amount of adsorbed dye increases, higher current density can be produced because of more light harvesting.

Although the efficiency of the fabricated all-oxide solid-state DSSCs slightly increases with nanorods length, we expected that the efficiency by the 7.5- and 6-μm-long Bi-doped TiO_2 nanorods would be increased much more than 17 and 7 % in comparison with that made from the 3.5-μm-long nanorods. This is due to the incomplete filling of the TiO_2 pores with solid-state electrolyte. Incomplete pore-filling is a major factor that limits the performance of the all-oxide solid-state DSSCs when the thickness of the photoanode is beyond 2 μm [45, 46]. The difficulties in effective pore-filling of the nanorods (or nanostructures) with high aspect ratios are still challenging. Previously, by controlling the initiated chemical vapor deposition (iCVD) condition, Nejati et al. [25] achieved to complete pore-filling for TiO_2 photoanode thicknesses up to 12 μm. A multistep pore-filling procedure was developed by Xu et al. [15] which is able to effectively fill spiro-OMeTAD into the TiO_2 nanowire arrays as thick as 50 μm. In order to improve the pore-filling in all-oxide solid-state DSSCs made from long nanorods, we pressed the fabricated device by hydraulic press. Mechanical pressing can improve the pore-filling of mesoporous photoanode by the $CuCrO_2$ nanoparticles and also improve the interparticle contact between the nanoparticles. In this way, the interparticle electrical conductivity can be enhanced by mechanical sintering.

J–V characteristic curves of the fabricated SS-DSSCs with 7.5-μm-long Bi-doped TiO_2 (3 %) nanorod arrays before and after pressing are shown in Fig. 8a. Device A (before pressing) exhibits an η of 0.120 %, corresponding to a V_{OC} of 348 mV, J_{SC} of 890 μA/cm^2 and FF of 36.8, and Device B (after pressing) shows a V_{OC} of 368 mV, J_{SC} value of 1.24 mA/cm^2 and FF of 45.3, yielding an η of 0.205 %. These obtained results demonstrate that the pressing of the solid-state DSSC enhances its photovoltaic performance. The higher performance of Device B in comparison with Device A is mainly due to the increase in the value of the short-circuit current density and the improvement of the fill factor. In order to elucidate the reasons of the improvement of the J_{SC} and FF, we briefly describe the mechanism of the pore-filling. The procedure of the pore-filling is initiated by spin coating a solution of the nanoparticles in ethanol onto the dye-sensitized nanorod arrays. After deposition, the solution fills the nanoscale space between nanorods, effectively. The wet

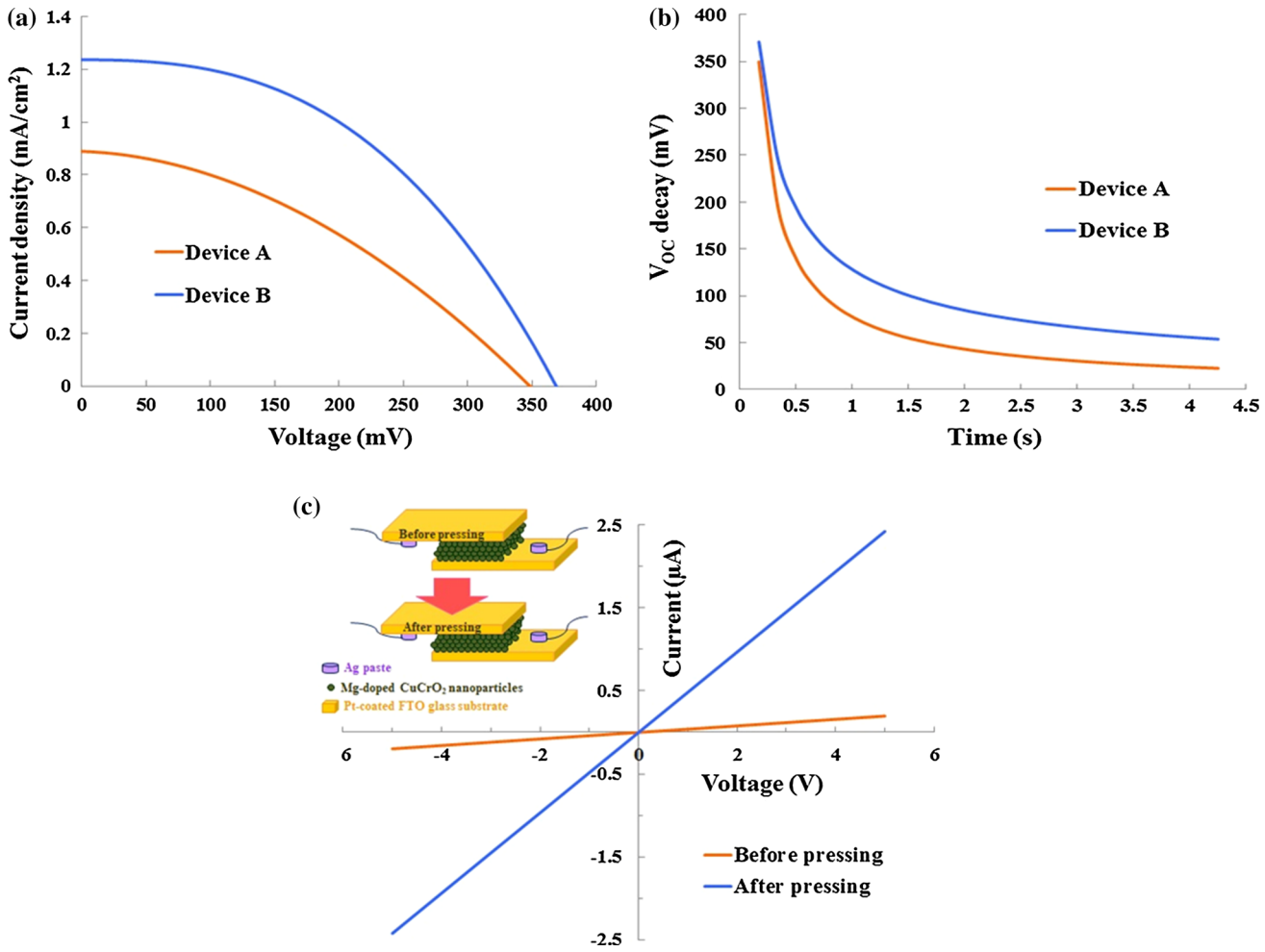

Fig. 8 **a** Current density–voltage curves and **b** open-circuit photovoltage decay measurement of the DSSCs assembled from Bi-doped TiO_2 (3 %) nanorod arrays and Mg-doped $CuCrO_2$ nanoparticles before (Device A) and after (Device B) pressing under simulated AM1.5 solar light (100 mW/cm^2). **c** I–V curves of Mg-doped $CuCrO_2$ nanoparticles

layer of the solution on top of the dye-sensitized nanorod arrays acts as a reservoir to increase the filling fraction (volume fraction of the nanoscale space between nanorods filled by the nanoparticles), so that as ethanol evaporates and the solution concentration increases, more nanoparticles penetrate into the space between nanorods. This penetration procedure is stopped when a large amount of ethanol is evaporated and the nanoparticles become immobile. After that, the penetration depth of the nanoparticles further increases by mechanical pressing of the nanoparticles. Furthermore, the contact between the nanoparticles and between the particles and the dye-sensitized nanorod arrays is improved by pressing. The electrical conductivity of the Mg-doped $CuCrO_2$ nanoparticles increases by the formation of large necks between adjacent particles because of the mechanical sintering through pressing. The penetration depth and the filling fraction are two important factors of pore-filling in solid-state DSSCs [13, 14]. Deep penetration depth of the nanoparticles facilitates the regeneration of the excited N719 dye molecules in the bottom of the photoanode by transferring holes to the nanoparticles and contributing to the generation of the photocurrent [46]. High filling fraction leads to the reduction in recombination and series resistance and subsequently improves the fill factor [25, 47, 48]. Regarding these reasons, the significant improvement in the photovoltaic parameters of the Device B can be ascribed to the improvement of the dye regeneration and/or charge collection due to the improvement of the pore-filling of the space between the nanorods by the nanoparticles. In order to have a better insight into the charge transport and recombination processes within the all-oxide solid-state DSSCs, the open-circuit photovoltage decay of the devices has been measured before and after pressing. The plot of the photovoltage decay as a function of time is shown in Fig. 8b. As can be seen, the decay of the open-circuit photovoltage in the Device B is slower than that in Device A which indicates that the pressing of the all-oxide solid-

state DSSCs is an effective method for reduction in the charge recombination rate at the interface. The observed slower recombination rate in Device B can be explained by faster charge transport through the mechanically sintered and interconnected Mg-doped $CuCrO_2$ nanoparticles. In order to exhibit the charge transport improvement in the sintered and interconnected nanoparticles, electrical conductivity measurement has also been performed on the nanoparticles. I–V characteristic curves of the Mg-doped $CuCrO_2$ nanoparticles between two Pt-coated FTO substrates before and after pressing (in the same condition for preparing Device A and B) are shown in Fig. 8c. The obtained results exhibit that the fabricated structures have ohmic contact behavior and reveal that the electrical conductivity of the nanoparticles increases by pressing. A two-step transport mechanism can be considered for charge carrier in Mg-doped $CuCrO_2$ nanoparticles. Initially, electrons diffuse inside one particle. After reaching the surface of the particle, they transfer from the particle to the neighboring one through a neck formed between them [49, 50]. According to this description, it can be concluded that the formation of the large neck between adjacent nanoparticles by mechanical sintering is desirable for good electron transport. In conclusion, the slower electron recombination and faster electron transport in Device B have led to 40, 6 and 71 % increase in J_{SC}, V_{OC} and η, respectively. Recently, Pavan et al. prepared the TiO_2/Cu_2O all-oxide heterojunction solar cells by spray pyrolysis method onto FTO glass substrates with short-circuit current density of 0.4 mA/cm^2 and open-circuit voltage about 350 mV [51]. Furthermore, Yuhas et al. [52] have observed photovoltaic properties in FTO/ZnO nanowire/Cu_2O nanoparticles structure with energy conversion efficiency of about 0.053 % by using a TiO_2 blocking layer.

4 Conclusions

Vertically aligned Bi-doped TiO_2 nanorod arrays with different lengths as photoanodes were successfully grown on FTO substrates by hydrothermal method. Furthermore, Mg-doped $CuCrO_2$ nanoparticles with *p*-type conductivity were synthesized by sol–gel method as solid-state electrolyte. It was shown that the diameter of the nanorods was increased with bismuth doping concentration. The fabricated all-oxide solid-state DSSCs with 3 % Bi-doped TiO_2 nanorods revealed maximum efficiency in comparison with the other cells due to the higher dye loading, slower charge recombination rate and the higher electrical conductivity of the 3 % Bi-doped TiO_2 nanorods. In order to increase the pore-filling and enable the use of nanorods with a long length in all-oxide solid-state DSSCs, the pressing technique was employed. The obtained results demonstrated that the pressing of the solid-state DSSC enhances its photovoltaic performance due to the improvement of both the interparticle contact and electrical conductivity. The higher performance of the pressed solid-state DSSC in comparison with unpressed ones is mainly due to the increase in the value of the short-circuit current density and the improvement of the fill factor.

Acknowledgments We gratefully acknowledge financial support from the Iran National Science Foundation (INSF), under Grant Number 93034818.

References

1. C.Y. Hsu, Y.C. Chen, R.Y.Y. Lin, K.C. Hob, J.T. Lin, Phys. Chem. Chem. Phys. **14**, 14099 (2012)
2. M. Adineh, P. Tahay, M. Ameri, N. Safari, E. Mohajerani, RSC Adv. **6**, 14512 (2016)
3. S. Powar, D. Xiong, T. Daeneke, M.T. Ma, A. Gupta, G.P. Lee, S. Makuta, Y. Tachibana, W. Chen, L. Spiccia, Y.B. Cheng, G. Gotz, P. Bauerle, U. Bach, J. Phys. Chem. C **118**, 16375 (2014)
4. D. Xiong, Z. Xu, X. Zeng, W. Zhang, W. Chen, X. Xu, M. Wang, Y.B. Cheng, J. Mater. Chem. **22**, 24760 (2012)
5. C.G. Ezema, A.C. Nwanya, B.E. Ezema, B.H. Patil, R.N. Bulakhe, P.O. Ukoha, C.D. Lokhande, M. Maaza, F.I. Ezema, Appl. Phys. A **122**, 435 (2016)
6. S. Mathew, A. Yella, P. Gao, R. Humphry-Baker, B.F.E. Curchod, N. Ashari-Astani, I. Tavernelli, U. Rothlisberger, M.K. Nazeeruddin, M. Gratzel, Nat. Chem. **6**, 242 (2014)
7. H. Li, S. Li, Y. Zhang, F. Yan, RSC Adv. **6**, 346 (2016)
8. I.K. Ding, J. Melas-Kyriazi, N.L. Cevey-Ha, K.G. Chittibabu, S.M. Zakeeruddin, M. Gratzel, M.D. McGehee, Org. Electron. **11**, 1217 (2010)
9. C.P. Lee, L.Y. Lin, P.Y. Chen, R. Vittal, K.C. Ho, J. Mater. Chem. **20**, 3619 (2010)
10. V. Armel, M. Forsyth, D.R. MacFarlane, J.M. Pringle, Energy Environ. Sci. **4**, 2234 (2011)
11. S.Y. Cha, Y.G. Lee, M.S. Kang, Y.S. Kang, J. Photochem. Photobiol., A **211**, 193 (2010)
12. Y. Zhang, J. Zhao, B. Sun, X. Chen, Q. Li, L. Qiu, F. Yan, Electrochim. Acta **61**, 185 (2012)
13. H. Wang, X. Zhang, F. Gong, G. Zhou, Z.S. Wang, Adv. Mater. **24**, 121 (2012)
14. J.H. Yum, P. Chen, M. Gratzel, M.K. Nazeeruddin, ChemSusChem **1**, 699 (2008)
15. C. Xu, J.n Wu, U. V. Desai, D. Gao. Nano Lett. **12**, 2420 (2012)
16. Y. Wang, P. Sun, S. Cong, J. Zhao, G. Zou, Carbon **92**, 262 (2015)
17. J. Bandara, J.P. Yasomanee, Semicond. Sci. Technol. **22**, 20 (2007)
18. S.J. Lim, Y.S. Kang, D.W. Kim, Electrochim. Acta **56**, 2031 (2011)
19. S. Yuan, Q. Tang, B. Hu, C. Ma, J. Duan, B. He, J. Mater. Chem. A **2**, 2814 (2014)
20. J. Zhao, X. Shen, F. Yan, L. Qiu, S. Lee, B. Sun, J. Mater. Chem. **21**, 7326 (2011)
21. S.R. Jang, K. Zhu, M.J. Ko, K. Kim, C. Kim, N.G. Park, A.J. Frank, ACS Nano **5**, 8267 (2011)
22. B. O'Regan, D.T. Schwartz, S.M. Zakeeruddin, M. Gratzel, Adv. Mater. **12**, 1263 (2000)
23. P.M. Sirimanne, T. Jeranko, P. Bogdanoff, S. Fiechter, H. Tributsch, Semicond. Sci. Technol. **18**, 708 (2003)

24. E.V.A. Premalal, R.M.G. Rajapakse, A. Konno, Electrochim. Acta **56**, 9180 (2011)
25. S. Nejati, K.K.S. Lau, Nano Lett. **11**, 419 (2011)
26. T. Leijtens, I.K. Ding, T. Giovenzana, J.T. Bloking, M.D. McGehee, A. Sellinger, ACS Nano **6**, 1455 (2012)
27. C. Cetin, H. Akyildiz, Mater. Chem. Phys. **170**, 138 (2016)
28. M. Asemi, M. Ghanaatshoar, Ceram. Int. **42**, 6664 (2016)
29. B. Liu, E.S. Aydil, J. Am. Chem. Soc. **131**, 3985 (2009)
30. C. Nithya, ChemPlusChem **80**, 1000 (2015)
31. H. Wang, L. Xi, J. Tucek, C. Ma, G. Yang, M.K.H. Leung, R. Zboril, C. Niu, A.L. Rogach, ChemElectroChem **1**, 1563 (2014)
32. H.A. Hamedani, N.K. Allam, M.A. El-Sayed, M.A. Khaleel, H. Garmestani, F.M. Alamgir, Adv. Funct. Mater. **24**, 6783 (2014)
33. S. Xiao, L. Zhao, J. Lian, Catal. Lett. **144**, 347 (2014)
34. Z. Liang, H. Cui, K. Wang, P. Yang, L. Zhang, W. Mai, C.X. Wang, P. Liu, CrystEngComm **14**, 1723 (2012)
35. M. Asemi, M. Ghanaatshoar, J. Sol-Gel. Sci. Technol. **70**, 416 (2014)
36. M. Niu, R. Cui, H. Wu, D. Cheng, D. Cao, J. Phys. Chem. C **119**, 13425 (2015)
37. H. Zuo, J. Sun, K, Deng, R. Su, F. Wei and D. Wang. Chem. Eng. Technol. **30**, 577 (2007)
38. A. Zaban, M. Greenshtein, J. Bisquert, ChemPhysChem **4**, 859 (2003)
39. K. Wijeratne, J. Akilavasan, M. Thelakkat, J. Bandara, Electrochim. Acta **72**, 192 (2012)
40. J.J. Wu, G.R. Chen, H.H. Yang, C.H. Ku, J.Y. Lai, Appl. Phys. Lett. **90**, 213109 (2007)
41. M.S. Liang, C.C. Khaw, C.C. Liu, S.P. Chin, J. Wang, H. Li, Ceram. Int. **39**, 1519 (2013)
42. S. So, K. Lee, P. Schmuki, Phys. Status Solidi RRL **6**, 169 (2012)
43. J. Liu, H. Yang, W. Tan, X. Zhou, Y. Lin, Electrochim. Acta **56**, 396 (2010)
44. L. Schlur, A. Carton, P. Leveque, D. Guillon, G. Pourroy, J. Phys. Chem. C **117**, 2993 (2013)
45. J. Melas-Kyriazi, I.K. Ding, A. Marchioro, A. Punzi, B.E. Hardin, G.F. Burkhard, N. Tetreault, M. Gratzel, J.E. Moser, M.D. McGehee, Adv. Energy Mater. **1**, 407 (2011)
46. H.J. Snaith, R. Humphry-Baker, P. Chen, I. Cesar, S.M. Zakeeruddin, M. Gratzel, Nanotechnology **19**, 424003 (2008)
47. M. Gao, Y. Wang, Q. Yi, Y. Su, P. Sun, X. Wang, J. Zhao, G. Zou, J. Mater. Chem. A **3**, 20541 (2015)
48. I.K. Ding, N. Tetreault, J. Brillet, B.E. Hardin, E.H. Smith, S.J. Rosenthal, F. Sauvage, M. Gratzel, M.D. McGehee, Adv. Funct. Mater. **19**, 2431 (2009)
49. K. Park, Q. Zhang, D. Myers, G. Cao, Appl. Mater. Interfaces **5**, 1044 (2013)
50. G. Benko, B. Skarman, R. Wallenberg, A. Hagfeldt, V. Sundstrom, A.P. Yartsev, J. Phys. Chem. B **107**, 1370 (2003)
51. M. Pavan, S. Rühle, A. Ginsburg, D.A. Keller, H.N. Barad, P.M. Sberna, D. Nunes, R. Martins, A.Y. Anderson, A. Zaban, E. Fortunato, Sol. Energ. Mater. Sol. Cells **132**, 549 (2015)
52. B.D. Yuhas, P. Yang, J. Am. Chem. Soc. **131**, 3756 (2009)